Title

Efficient system modeling for a small animal PET scanner with tapered DOI detectors

Journal

Physics in Medicine and Biology, 61(2)

ISSN

0031-9155

Authors

Zhang, Mengxi
Zhou, Jian
Yang, Yongfeng
et al.

Publication Date

2016-01-21

DOI

10.1088/0031-9155/61/2/461

Peer reviewed

HHS Public Access

Author manuscript

Phys Med Biol. Author manuscript; available in PMC 2017 January 21.

Published in final edited form as:

Phys Med Biol. 2016 January 21; 61(2): 461–474. doi:10.1088/0031-9155/61/2/461.

Efficient system modeling for a small animal PET scanner with tapered DOI detectors

Mengxi Zhang[1], **Jian Zhou**[1], **Yongfeng Yang**[1], **Mercedes Rodríguez-Villafuerte**[2], and **Jinyi Qi**[1]

Jinyi Qi: qi@ucdavis.edu

[1]Department of Biomedical Engineering, University of California-Davis, One Shields Avenue, Davis, CA 95616, USA

[2]Instituto de Física, Universidad Nacional Autónoma de México, A. P. 20–364, 01000, Mexico D. F., Mexico

Abstract

A prototype small animal positron emission tomography (PET) scanner for mouse brain imaging has been developed at UC Davis. The new scanner uses tapered detector arrays with depth of interaction (DOI) measurement. In this paper, we present an efficient system model for the tapered PET scanner using matrix factorization and a virtual scanner geometry. The factored system matrix mainly consists of two components: a sinogram blurring matrix and a geometrical matrix. The geometric matrix is based on a virtual scanner geometry. The sinogram blurring matrix is estimated by matrix factorization. We investigate the performance of different virtual scanner geometries. Both simulation study and real data experiments are performed in the fully 3D mode to study the image quality under different system models. The results indicate that the proposed matrix factorization can maintain image quality while substantially reduce the image reconstruction time and system matrix storage cost. The proposed method can be also applied to other PET scanners with DOI measurement.

Keywords

positron emission tomography; image reconstruction; system modeling

1. Introduction

High sensitivity and high spatial resolution are critical in positron emission tomography (PET) system design. High sensitivity can increase signal-to-noise ratio (SNR) and reduce both injected dose and scan time, while high spatial resolution allows visualization of fine details in PET images. The spatial resolution of PET scanners is affected by several factors. In the image domain, positron range (the distance that a positron travelled before it annihilates with an electron) and photon non-collinearity (the two photons are not emitted exactly 180 degrees apart) introduce blurring to the underlying PET tracer distribution. In the detector front, when a 511 keV photon enters a long crystal at an oblique angle, it can penetrate multiple crystal elements and results in mispositioning of the coincidence event. This is commonly known as the parallax error, which leads to worse spatial resolution

towards the edge of the transaxial field of view (FOV). The parallax error is a major problem in small animal PET scanners with a compact geometry.

Both hardware and software approaches have been proposed to reduce the blurring effects in PET images. One of the software approaches is resolution modeling in an iterative reconstruction framework, where a system matrix that maps from the image space to the projection space can be used to accurately model the system response. Analytical models have been developed to include the solid angle and crystal penetration effects, e.g. (Huesman *et al* 2000). To reduce the storage size and computational time, factored system matrices can be used to model the blurring effects in either the image space, or the projection space, or both. Image space modeling fits the point spread function (PSF) in reconstructed images and incorporates the image domain PSF into the forward and back projections (Reader *et al* 2013). It can be easily implemented without much increase of computational cost and is compatible with list-mode image reconstruction. However, the effects of parallax error and inter-crystal scatters are easier to model in the projection space. The projection space blurring model can be obtained either from Monte Carlo simulation (Qi *et al* 1998, Alessio *et al* 2006), or from real point source measurements (Tohme and Qi 2009).

These improved system models can enhance spatial resolution. As a result, lesion detection performance is improved. The complexity of system matrix also increases computational cost and slow the convergence speed, but it can be overcome by modern computer technology, such as computer clusters or graphic processing units (GPU) (Pratx *et al* 2009, Zhou and Qi 2011).

Depth of interaction (DOI) measurement is a hardware approach to improve spatial resolution. PET systems with DOI information can correct parallax error, and hence have better spatial resolution and resolution uniformity. Furthermore, the cost of the system can be reduced by building a scanner with a smaller ring diameter for the same FOV. Multiple methods have been developed to obtain DOI measurements.

Discrete DOI can be obtained by using multiple layers of crystals. Each crystal can be read out individually (Levin 2002, Rafecas *et al* 2003) for the best performance, or the interactions in each layer can be discriminated by pulse shape (Mosset *et al* 2006, deJong *et al* 2007), or by crystal offset (Zhang *et al* 2003). Continuous DOI can be measured by using dual-ended readout (Shao *et al* 2002, Godinez *et al* 2012) and calculating the ratio between one readout signal and the summation of two readout signals. The continuous DOI information can also be extracted from the light dispersion (Ling *et al* 2007).

DOI detectors have been incorporated in several commercialized PET scanners. The ECAT high-resolution research tomography (HRRT) is a human brain scanner and is the first commercially available DOI-PET scanner (Wienhard *et al* 2002). General electric small animal PET scanner eXplore Vista uses a double layer of LYSO/GSO crystals (Wang *et al* 2006). The Shimazu Clairvivo small animal PET employs crystal offset method in the axial direction (Mizuta *et al* 2008).

The prototype small animal PET scanner for mouse brain imaging at UC Davis uses detector arrays with dual-ended readout (Yang *et al* 2008). The detectors are coupled to position

sensitive avalanche photodiodes (PSAPDs) on both ends. Due to the dead space of PSAPDs, the area of PSAPD is larger than that of the detector block, which leads to large gaps between detector blocks. Hence, the crystals are manufactured into a tapered shape along the radial direction to increase sensitivity. One of the challenges in image reconstruction for the tapered DOI-PET scanner is that the number of DOI-based line of response increases proportionally to the square of the number of DOI bins. Therefore, the size of the system matrix of a DOI-PET scanner is much larger than that of a non-DOI PET scanner.

There are several existing methods for DOI compression based on DOI data redundancy, i.e. lines of response among neighboring DOI bins are highly correlated. One option is rebinning rear DOI bins into front DOI bins and uses a precomputed system (Yamaya *et al* 2003, 2008). This method, however, does not work well in our case because of the large gaps between detector blocks.

In order to reduce the storage space and computational time without degradation of image quality, we propose to use a factored system matrix for our tapered scanner. The factored system matrix mainly consists of two components: a sinogram blurring matrix and a geometrical matrix. Unlike most factored system models in which the geometric projection matrix was defined by the original scanner geometry, the geometric projection matrix in this paper is computed based on a virtual scanner geometry, which provides not only more freedom in the calculation of the geometric projection matrix but also the necessary coverage between detector gaps. While virtual scanner geometry has been proposed before for image reconstruction (Scheins *et al* 2007), we focus here on combining it with a factored system matrix. The sinogram blurring matrix maps the virtual sinogram to the physical sinogram and is estimated by matrix factorization (Zhou and Qi 2010). We studied different virtual crystal sizes, different virtual geometry, and the effect of the blurring matrix.

The rest of this paper is organized as follows. We introduce the system matrix calculation and factorization in section 2. Section 3 describes the geometry of both physical detectors and virtual detectors, as well as the experiments for validation. Reconstructed images and quantitative analysis are shown in section 4. Finally, conclusions are presented in section 5.

2. Method

2.1. Scanner geometry

The prototype scanner contains 16 detectors forming a 62.5 mm inner diameter ring. Each detector contains a 14 × 14 array of LSO crystals. Each crystal element has a front face of $0.5 \times 0.5\ mm^2$, a back face of $0.5 \times 0.875\ mm^2$, and is 13 mm long along the radial direction, as shown in figure 1. The detector blocks are coupled to PSAPDs on both ends to decode DOI information (Yang *et al* 2008). The FOV of the scanner is about 30 mm in diameter.

2.2. The system matrix

The (i, j)th element $p_{i,j}$ of $\boldsymbol{P} \in \mathbb{R}^{M \times N}$ denotes the probability of detecting an emission from pixel j, $j \in 1,\ldots, N$, at detector pair i, $i \in 1, \ldots, M$. The accurate system matrix in this work is calculated analytically by dividing each crystal element into a large number of sub-

crystals (Huesman *et al* 2000). For each DOI bin, a Gaussian profile with the full-width-at-half-maximum (FWHM) equals to the measured DOI resolution is used to weight the contribution of each sub-crystal (Yang *et al* 2008). Hence, the crosstalk between DOI bins is included in the model. To reduce the storage size and computational cost, we factor the system matrix $\boldsymbol{P}$ as $\boldsymbol{P} = \boldsymbol{BG}$, where $\boldsymbol{B}$ is the sinogram blurring matrix and $\boldsymbol{G}$ is the virtual geometrical projection matrix.

The virtual geometrical matrix was computed using 16 virtual detectors made of a perfect absorber, forming a 62.5 mm diameter ring. The virtual detectors can have an arbitrary size. We studied 5 different virtual crystal sizes: 0.216 mm, 0.25 mm (half of the front size of the real crystal), 0.325 mm, 0.433 mm, and 0.5 mm. For the final reconstructions, we choose 0.216 mm as the virtual crystal size in the transaxial direction and 0.25 mm in the axial direction, which is about half of the physical crystal size. As a result, each virtual detector block consists of 56 × 28 virtual detector elements and there is no gap between adjacent virtual detector blocks. The accurate system matrix $\boldsymbol{P}$ was computed by tracing $(5 \times 5 \times 100)^2$ (transaxial × axial × depth) rays with the end points uniformly distributed in the two physical crystals forming each line of response (LOR) and matrix $\boldsymbol{G}$ was computed by tracing $(5 \times 5 \times 1)^2$ rays between each pair of virtual crystals.

To further reduce the computational cost and storage size, we performed an angular down-sampling operation on the virtual system matrix $\boldsymbol{G}$, by which the number of angular views is reduced by half. Therefore, the sizes of both the sinogram blurring matrix and the virtual geometric projection matrix are reduced by a factor of 2, and the computational cost of image reconstruction is expected to be reduced by the same factor.

2.3. Estimation of the sinogram blurring matrix

For a given virtual geometric projection matrix $\boldsymbol{G}$, we estimate $\boldsymbol{B}$ by

$$\hat{\boldsymbol{B}} = \arg\min_{\boldsymbol{B}\geq 0} \Phi(\boldsymbol{P}, \boldsymbol{BG}), \quad (1)$$

where Φ is the Kullback–Leibler (KL) distance which is defined as

$$\Phi(\boldsymbol{Y}, \boldsymbol{X}) \triangleq -\sum_{m,n} \left\{ [\boldsymbol{Y}]_{m,n} \log\left(\frac{[\boldsymbol{Y}]_{m,n}}{[\boldsymbol{X}]_{m,n}} \right) + [\boldsymbol{X}]_{m,n} - [\boldsymbol{Y}]_{m,n} \right\}, \quad (2)$$

with $[\boldsymbol{X}]_{m,n}$ being the (m, n)th element of matrix $\boldsymbol{X}$. By substituting (2) into (1) and removing terms independent of $\boldsymbol{B}$, we have

$$\hat{\boldsymbol{B}} = \arg\min_{\boldsymbol{B}\geq 0} \sum_{m,n} \{ [\boldsymbol{BG}]_{m,n} - [\boldsymbol{P}]_{m,n} \log([\boldsymbol{BG}]_{m,n}) \} = \arg\min_{\boldsymbol{B}\geq 0} \sum_{m,n} \left\{ \left[\boldsymbol{G}^T (\boldsymbol{B}_{m,\cdot})^T \right]_n - [\boldsymbol{P}]_{m,n} \log\left(\left[\boldsymbol{G}^T (\boldsymbol{B}_{m,\cdot})^T \right]_n \right) \right\} \quad (3)$$

where $\boldsymbol{B}_{m,\cdot}$ represents the mth row of matrix $\boldsymbol{B}$ and $[\boldsymbol{x}]_n \triangleq x_n$ denotes the nth entry of vector $\boldsymbol{x}$. The superscript 'T' represents vector or matrix transpose. Note that each row of $\boldsymbol{B}$ can be estimated separately via

$$(\hat{\boldsymbol{B}}_{m,\cdot})^T = \arg\min_{\boldsymbol{x}\geq 0} \sum_n \left([\boldsymbol{G}^T\boldsymbol{x}]_n - [\boldsymbol{P}]_{m,n} \log([\boldsymbol{G}^T\boldsymbol{x}]_n) \right) \quad (4)$$

Equation (4) shares the same form as the maximum likelihood (ML) image reconstruction for emission tomography, so we can solve (4) using the same ML expectation-maximization (EM) algorithm. Details can be found in references (Tohme and Qi 2009, Zhou and Qi 2011). In the experiments performed below, we ran 150 iterations of the ML EM algorithm to estimate the sinogram blurring matrix.

3. Simulation and real experiments

3.1. GATE simulation

To demonstrate the DOI benefits and validate that the proposed system matrix factorization method can preserve the spatial resolution, we simulated the geometry of the proposed small-animal scanner using the Geant4 Application for Emission Tomography (GATE) simulation code (Jan *et al* 2004). The timing window was 20 ns, the energy resolution was 25% and the energy window was set to 250–750 keV. The parameters were selected based on our previous work (Yang *et al* 2008, James *et al* 2009, Rodríguez-Villafuerte *et al* 2014). To evaluate the effect on image quality, we simulated a Derenzo phantom with hot rods sizes of 0.75 mm, 0.6 mm, 0.5 mm, 0.45 mm, 0.4 mm and 0.35 mm.

3.2. Point source acquisition

A 30 μCi ^{22}Na point source was scanned at 15 locations within the scanner as shown in figure 2 (at the axial center slice and ±¼ axial FOV with radial offsets of 0, 5, and 10 mm, respectively, along both vertical and horizontal directions). The ^{22}Na point source was encapsulated in Lucite and the active volume is about 0.3 mm in diameter. The small size makes the ^{22}Na point source a good choice for resolution measurement. Each position was scanned for 5 min. Projection of a uniform cylinder (background) was simulated and added to each point source data before reconstruction. The intensity ratio between the point source and the background was about 1.1 to 1 in the reconstructed images. We ran 700 iterations of the ML EM algorithm for each image reconstruction. The images were reconstructed using 149 × 149 × 29 pixels with a pixel size of 0.2 × 0.2 × 0.25 mm^3. The final point source images were obtained after subtracting the background-only reconstruction. FWHM of each point source was calculated by linear interpolation for quantitative analysis.

3.3. Normalization

A uniform cylinder phantom filled with 150 μCi ^{18}F-FDG was scanned for 4 h to obtain normalization data. The cylinder was 30 mm in diameter and 10 mm long axially, which covered the entire FOV of the scanner. Crystal efficiencies and geometric correction factors were estimated from the measured cylinder data using a ML estimation algorithm (Bai *et al* 2002).

4. Results

4.1. Study of different virtual crystal sizes

Figure 3 shows the reconstructed images of a simulated Derenzo phantom with the accurate system matrix, and factored system matrices with different virtual crystal sizes (top row). The bottom row contains the difference images between those in the top row and the reconstructed image with the accurate system matrix. The reconstruction algorithm was MLEM with 100 iterations. Although a larger virtual crystal size reduces the computational cost and storage size by reducing the number of LORs in the system matrix, there is a noticeable mismatch between the result of the accurate system model and that of the factored system model, for example, near the center of the 0.6 mm rods. For quantitative comparison, we computed the normalized root mean square error (NRMS) defined as

$$\mathrm{NRMS}=\sqrt{\frac{\sum_i (x_i - x_i^{\mathrm{true}})^2}{\sum_i (x_i^{\mathrm{true}})^2}} \quad (5)$$

where x is the reconstructed image from a factored system model and x^{true} is the reconstructed image from the accurate system model. Figure 4 shows that the NRMS value decreases as we reduce the virtual crystal size. To maintain the image quality, we choose 0.216 mm virtual crystal in the transaxial direction. This choice is also convenient for the angular down-sampling operation because the number of virtual crystals to form the ring without gaps is exactly four times of the number of physical crystals.

4.2. Effect of angular down-sampling

Figure 5 compares the estimated blurring kernels with and without the angular down-sampling. The nine kernels shown are for ring difference 3, projection angle 18, radial bins 11 to 19. For each kernel, the horizontal axis is the angular offset and the vertical axis is the radial offset. The value of the blurring kernel at each position represents the contribution from a virtual LOR to the reference physical LOR. With the angular down-sampling, the angular width (horizontal) of each blurring kernel size is reduced by half. This translates directly to savings in storage size and computation time.

Figure 6 compares the kernel profiles with and without angular down-sampling. For an easy comparison, the kernels without angular down-sampling operation were summed for every two columns (angles), based on the physical positions of the LORs. The red squares represent the angular down-sampling kernel profiles and the green circles represent the angular sum of the kernel without angular down-sampling. The left panel shows the angular (horizontal) profiles and the right panel shows the radial (vertical) profiles. The two sets of kernels roughly match each other. There are some differences between the profiles because the effect of the angular down-sampling cannot be modeled exactly by a simple summation. Since it is the accuracy of the forward projection that matters in image reconstruction, we calculate the root mean squared error of their resulting forward projections of a Deronzo phantom using the forward projection produced by the accurate system matrix as the reference. The normalized root mean squared errors of the forward projections are 1.1%

(without angular down-sampling) and 1.4% (with angular down-sampling), respectively. The resulting NRMS errors in reconstructed images are reported in section 4.4.

4.3. Real point source reconstruction

Figure 7 shows the reconstructed 15 point sources using the accurate system matrix, and factored system matrices with and without angular down-sampling respectively. The trans-axial profiles are plotted in figure 8 for comparison. There is no noticeable difference between the reconstructed results of the two factored models. For most point sources, the profiles are virtually identical among the three system models.

For quantitative analysis, all FWHMs along three directions were calculated and listed in tables 1 and 2, respectively. Most FWHM values from the three system models are the same with the maximum difference between the factored model and the non-factored model being around 6%. Therefore, the spatial resolution is well-preserved within the scanner FOV by the factored system matrix.

For comparison, we used the accurate system matrix model to reconstruct the point sources without DOI information. The reconstructed images are shown in figure 9. Because of the parallax error, the reconstructed point sources are significantly elongated along the radial direction as the point sources are placed toward the edge of the FOV. Hence, the spatial resolution of the reconstructed point sources are much worse than those reconstructed with DOI information, as shown in table 3.

Table 3 also includes the results of reconstructed point sources using only the three front DOI bins. Because the detectors are tapered, i.e. the transaxial crystal size of the front DOI bins are smaller than that of the rear DOI bins, FWHMs were improved by using events from the front DOI bins only. However, the sensitivity was reduced by 85%, i.e. only 15% of the total events remains.

4.4. Reconstruction without sinogram blurring matrix

To illustrate the importance of the sinogram blurring matrix, we performed a reconstruction using only the virtual geometric projection matrix, which was similar to the previous work on virtual scanner (Scheins *et al* 2007). To reconstruct the image with a virtual system matrix only, the first step is to bin the list mode data into the virtual sinogram data using the nearest neighbor method, i.e. for each event in the list mode data, we draw a line between the two interaction points based on the continuous DOI measurements, and find the virtual LOR that contains the line. To get the normalization factors, we forward projected a uniform cylinder using the accurate system matrix $\boldsymbol{P}$, and rebinned the sinogram of the uniform cylinder into the virtual sinogram using the nearest neighbor method. Due to the small size of the virtual crystal, some of the virtual LORs do not receive any events and are not included in the reconstruction. The same uniform cylinder was also forward projected using the virtual geometric projection matrix $\boldsymbol{G}$. The normalization factors were computed as the ratio between the rebinned sinogram and virtual geometric projection. Figure 10 shows the reconstructed images of the GATE simulated Derenzo phantom with different system matrices. The NRMS errors compared to the reconstructed image using the accurate system

matrix are 1.2% (BG), 1.4% (BGds) and 28% (without blurring matrix), respectively. Clearly, without the sinogram blurring matrix, there is significant image quality degradation due to the mismatch between the virtual system model and the physical system. The NRMS errors of the reconstructed image using the factored system matrices are comparable to those reported in section 4.2 for the projections. The 0.2% increase in the NRMS error by the angular down-sampling is well justified by the factor of 2 reduction in reconstruction time.

4.5. Computation time and storage size

Table 4 shows the storage sizes of different system matrices. All matrices were stored in the MATLAB sparse matrix format. By using the factored system matrix, we obtained a 4-fold reduction in storage space for the factored system model and 8-fold for the factored system model with angular down-sampling.

Table 5 compares the projection calculation speeds. Here the calculations of both forward and back projections were implemented in C++ code with parallel computation on a PC running 64-bit Linux with a dual eight-core 2GHz Intel(R) Xeon(R) processors. Each projection calculation time shown in the Table was an average of 5 runs. We see that the sinogram blurring operation takes a significant amount of computation time, because the physical sinogram has 81 DOI pairs and each physical LOR receives contribution from multiple virtual LORs. As a result, the speed up factor in forward and back projections is less than the reduction factor in storage size.

5. Conclusions

We have proposed an efficient factorized system model for image reconstruction for a DOI-capable tapered PET scanner. The factored system matrix contains a virtual geometrical projection matrix and a sinogram blurring matrix. The factored model reduces the storage cost by a factor of 8.8 and the image reconstruction time by a factor of 5.5. Quantitative study on real point source resolution shows that the performance of the proposed factored system matrix is almost the same as the accurate system matrix, and spatial resolution is well-preserved within the FOV. In addition, profiles of point sources and Derenzo hot rods did not show any noticeable difference. Therefore, the proposed matrix factorization can maintain image quality while substantially reduce the image reconstruction time and system matrix storage cost. We also demonstrate the importance of the sinogram blurring matrix by reconstruct images with the virtual detector only, showing there is significant degradation on image quality without using the sinogram blurring matrix. The proposed method can be applied to other DOI-capable PET scanners.

Acknowledgments

This work was supported by the National Institute of Biomedical Imaging and Bioengineering under grants R01 EB006109 and R01 EB000194.

References

Alessio A, Kinahan P, Lewellen T. Modeling and incorporation of system response functions in 3D whole body PET. IEEE Trans. Med. Imaging. 2006; 25:828–837. [PubMed: 16827484]

Bai B, et al. Model-based normalization for iterative 3D PET image reconstruction. Phys. Med. Biol. 2002; 47:2773–2784. [PubMed: 12200938]

deJong H, et al. Performance evaluation of the ECAT HRRT: an LSO-LYSO double layer high resolution, high sensitivity scanner. Phys. Med. Biol. 2007; 52:1505–1526. [PubMed: 17301468]

Godinez F, et al. Characterization of a high-resolution hybrid DOI detector for a dedicated breast PET/CT scanner. Phys. Med. Biol. 2012; 57:3435–3449. [PubMed: 22581109]

Huesman R, et al. List-mode maximum-likelihood reconstruction applied to positron emission mammography (PEM) with irregular sampling. IEEE Trans. Med. Imaging. 2000; 19:532–537. [PubMed: 11021696]

James SS, et al. Simulation study of spatial resolution and sensitivity for the tapered depth of interaction PET detectors for small animal imaging. Phys. Med. Biol. 2009; 55:63–74.

Jan S, Santin G, Strul G. GATE: a simulation toolkit for PET and SPECT. Phys. Med. Biol. 2004; 49:4543–4561. [PubMed: 15552416]

Levin C. Design of a high resolution and high sensitivity scintillation crystal array with nearly perfect light collection. IEEE Trans. Nucl. Sci. 2002; 49:2236–2243.

Ling T, Lewellen T, Miyaoka R. Improving the intrinsic spatial resolution performance of the continuous miniature crystal element (cMiCE) detector. IEEE Nuclear Science Symp. Conf. Record. 2007:4308–4313.

Mizuta T, et al. Performance evaluation of a high-sensitivity large-aperture small-animal PET scanner: ClairvivoPET. Ann. Nucl. Med. 2008; 5:447–455. [PubMed: 18600425]

Mosset J, et al. Development of an optimized LSO/LuYAP phoswich detector head for the lausanne clearPET demonstrator. IEEE Trans. Nucl. Sci. 2006; 53:25–29.

Pratx J, Chinn G, Olcott P, Levin C. Fast, accurate and shift-varying line projections for iterative reconstruction using the GPU. IEEE Trans. Med. Imaging. 2009; 3:435–445. [PubMed: 19244015]

Qi J, et al. High-resolution 3D Bayesian image reconstruction using the microPET small-animal scanner. Phys. Med. Biol. 1998; 43:1001–1013. [PubMed: 9572523]

Rafecas M, et al. Inter-crystal scatter in a dual layer, high resolution LSO-APD positron emission tomograph. Phys. Med. Biol. 2003; 48:821–848. [PubMed: 12701889]

Reader A, et al. EM algorithm system modeling by image-space techniques for PET reconstruction. IEEE Trans. Nucl. Sci. 2013; 50:1392–1397.

Rodríguez-Villafuerte M, Yang Y, Cherry SR. A Monte Carlo investigation of the spatial resolution performance of a small-animal PET scanner designed for mouse brain imaging studies. Phys. Med. 2014; 30:76–85. [PubMed: 23566478]

Scheins J, Axer M, Pietrzyk U, Herzog H. Virtual scanner geometry for iterative 3D PET reconstruction adaptable to complex and irregular scanner topologies. IEEE Nuclear Science Symp. Conf. Record. 2007:3458–3460.

Shao Y, et al. Dual APD array readout of LSO crystals. IEEE Trans. Nucl. Sci. 2002; 49:649–654.

Tohme M, Qi J. Iterative image reconstruction for positron emission tomography based on a detector response function estimated from point source measurements. Phys. Med. Biol. 2009; 54:3709–3725. [PubMed: 19478379]

Wang Y, et al. Performance evaluation of the GE healthcare eXplore VISTA dual-ring small-animal PET scanner. J. Nucl. Med. 2006; 47:1891–1900. [PubMed: 17079824]

Wienhard K, et al. The ECAT HRRT: performance and first clinical application of the new high resolution research tomograph. IEEE Trans. Nucl. Sci. 2002; 49:104–110.

Yamaya T, et al. DOI-PET image reconstruction with accurate system modeling that reduces redundancy of the imaging system. IEEE Trans. Nucl. Sci. 2003; 50:1404–1409.

Yamaya T, et al. First human brain imaging by the jPET-D4 prototype with a pre-computed system matrix. IEEE Trans. Nucl. Sci. 2008; 55:2482–2492.

Yang Y, et al. A prototype PET scanner with DOI-encoding detectors. J. Nucl. Med. 2008; 49:1132–1140. [PubMed: 18552140]

Zhang N, et al. A prototype modular detector design for high resolution positron emission mammography imaging. IEEE Trans. Nucl. Sci. 2003; 50:1624–1629.

Zhou J, Qi J. Efficient system modeling of a high-resolution zoom-in PET scanner. IEEE Nuclear Science Symp. Conf. Record (NSS/MIC). 2010:3501–3505.

Zhou J, Qi J. Fast and efficient fully 3D PET image reconstruction using sparse system matrix factorization with gpu acceleration. Phys. Med. Biol. 2011; 56:6739–6757. [PubMed: 21970864]

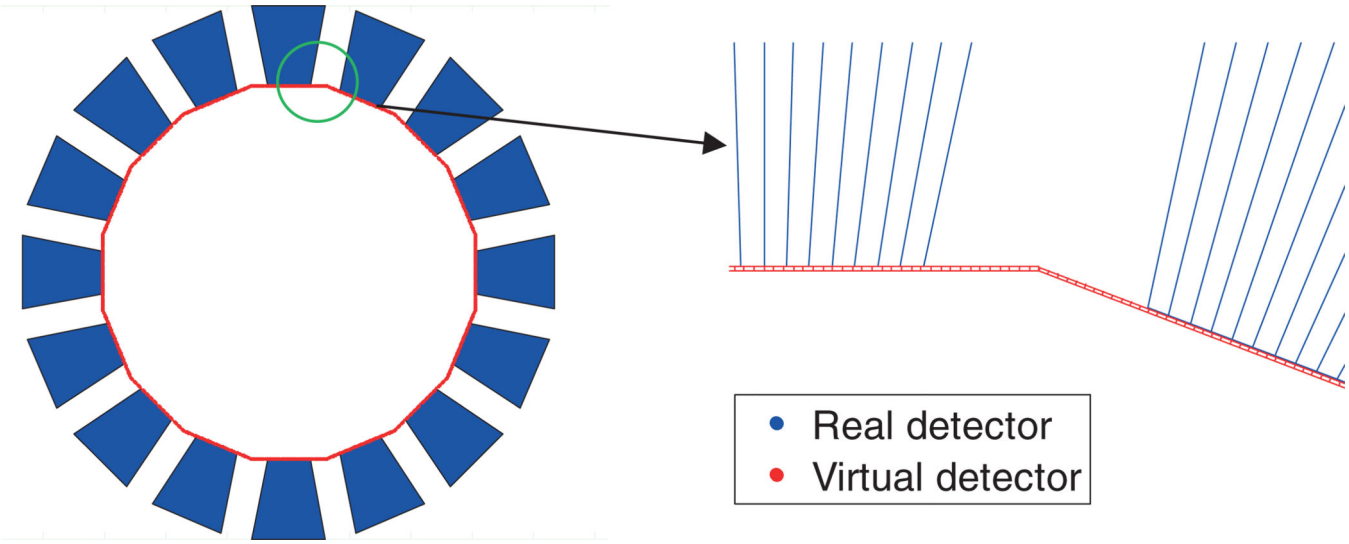

Figure 1.
Illustration of the physical and virtual scanner geometry in 2D.

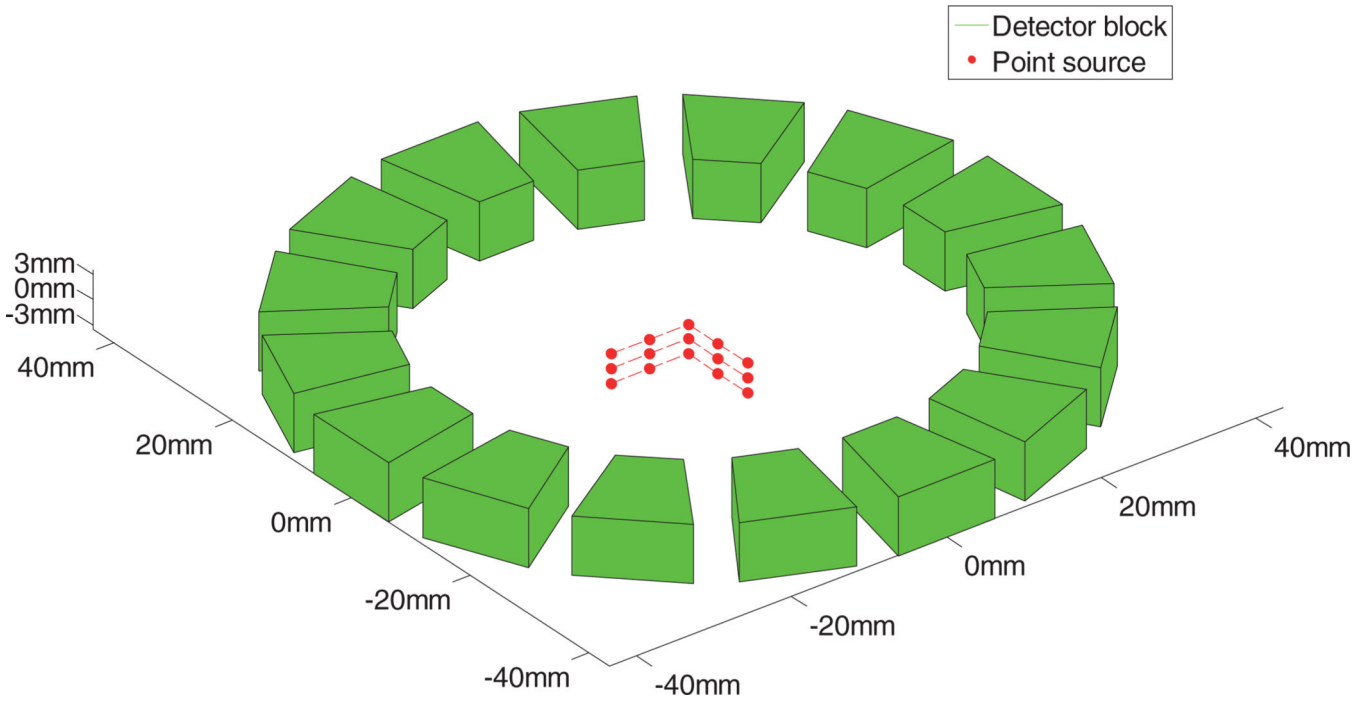

Figure 2.
Positions of the point source scans at the center and ±¼ axial FOV slices.

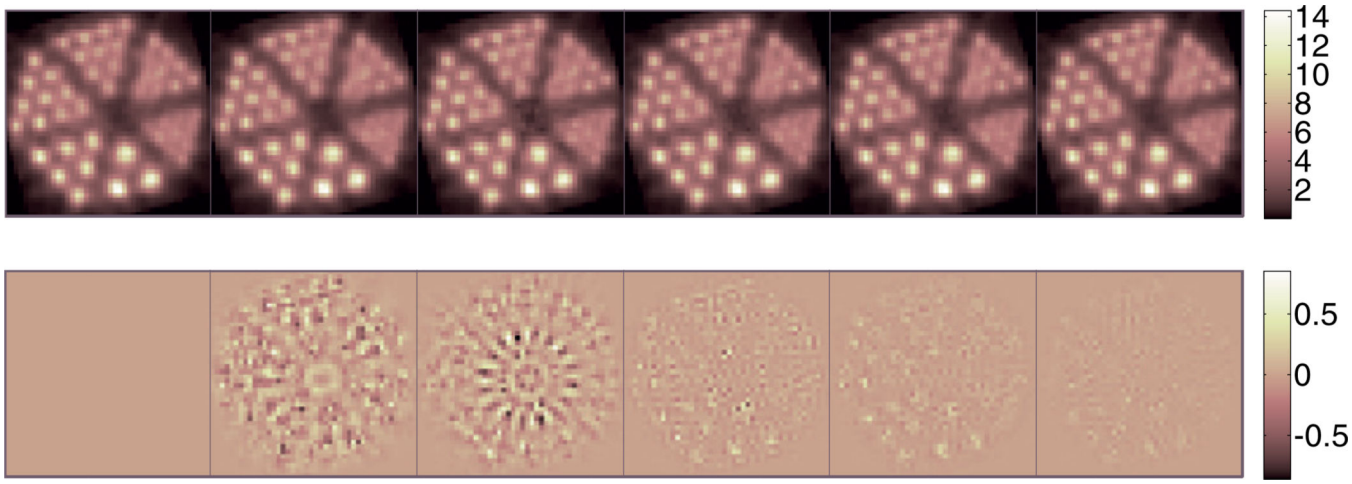

Figure 3.

Top row from left to right: Derenzo phantom reconstruction using the accurate system matrix and using the factorized system matrix with virtual crystal size of 0.5, 0.433, 0.325, 0.25, 0.216 mm, respectively. Bottom row: difference images between those in the top row and the reconstruction using the accurate system matrix (the first image).

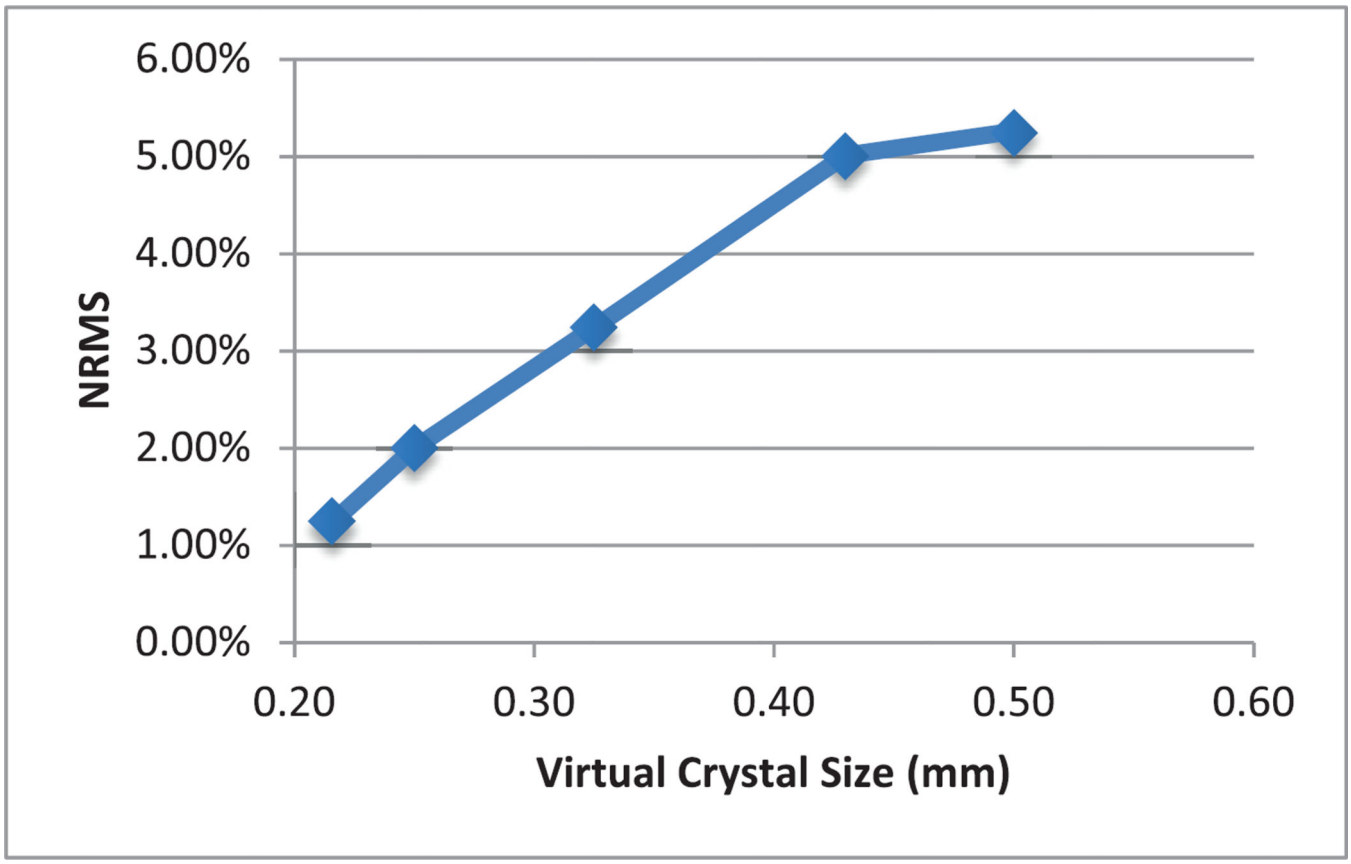

Figure 4.
NRMS as a function of the virtual crystal size.

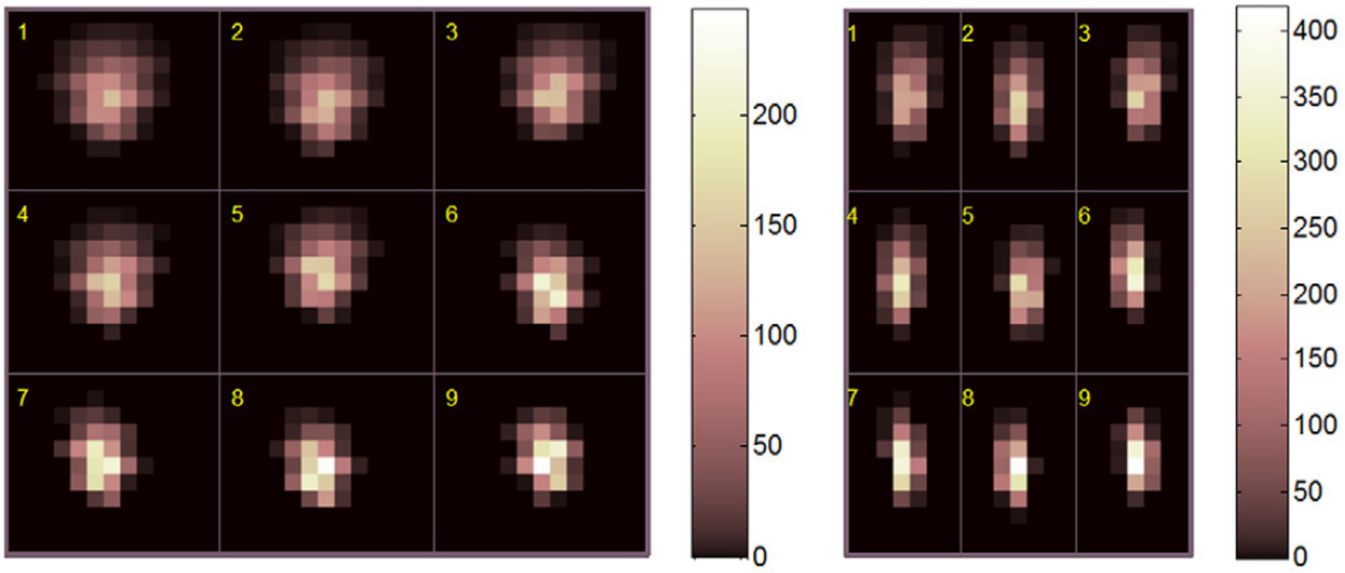

Figure 5.

Samples of blurring kernels for ring difference 3, projection angle 18, radial bins 11 to 19. Left: without angular down-sampling. Right: with angular down-sampling. Horizontal axis is the angular offset and the vertical axis is the radial offset.

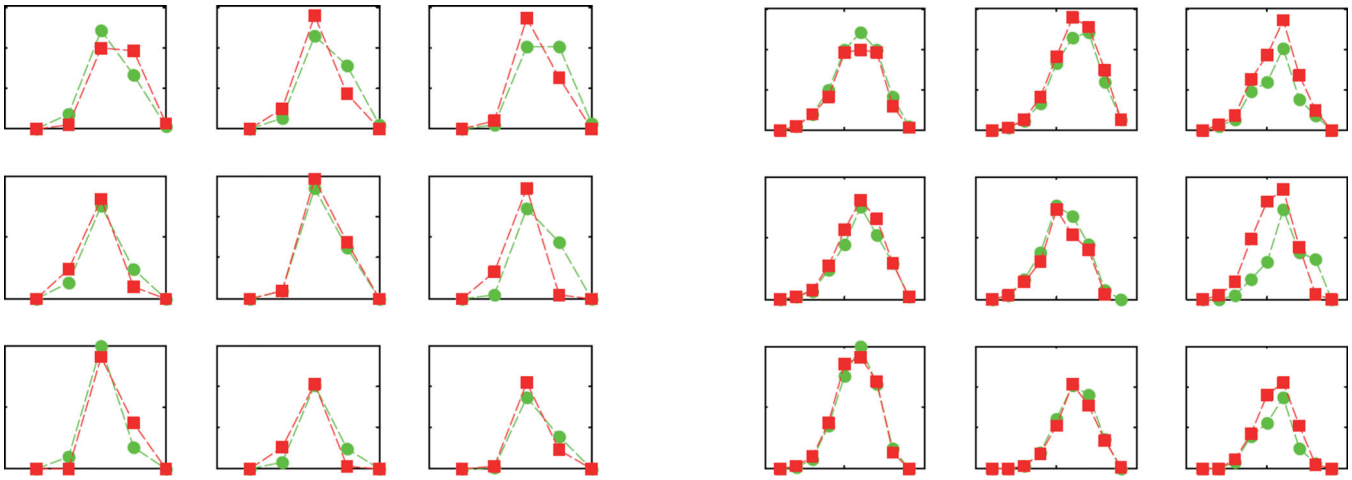

Figure 6.

Blurring kernel profiles. Left: angular (horizontal) profiles. Right: radial (vertical) profiles. Green circle: summation of neighboring columns of kernels without angular down sample. Red square: kernels with angular down-sampling.

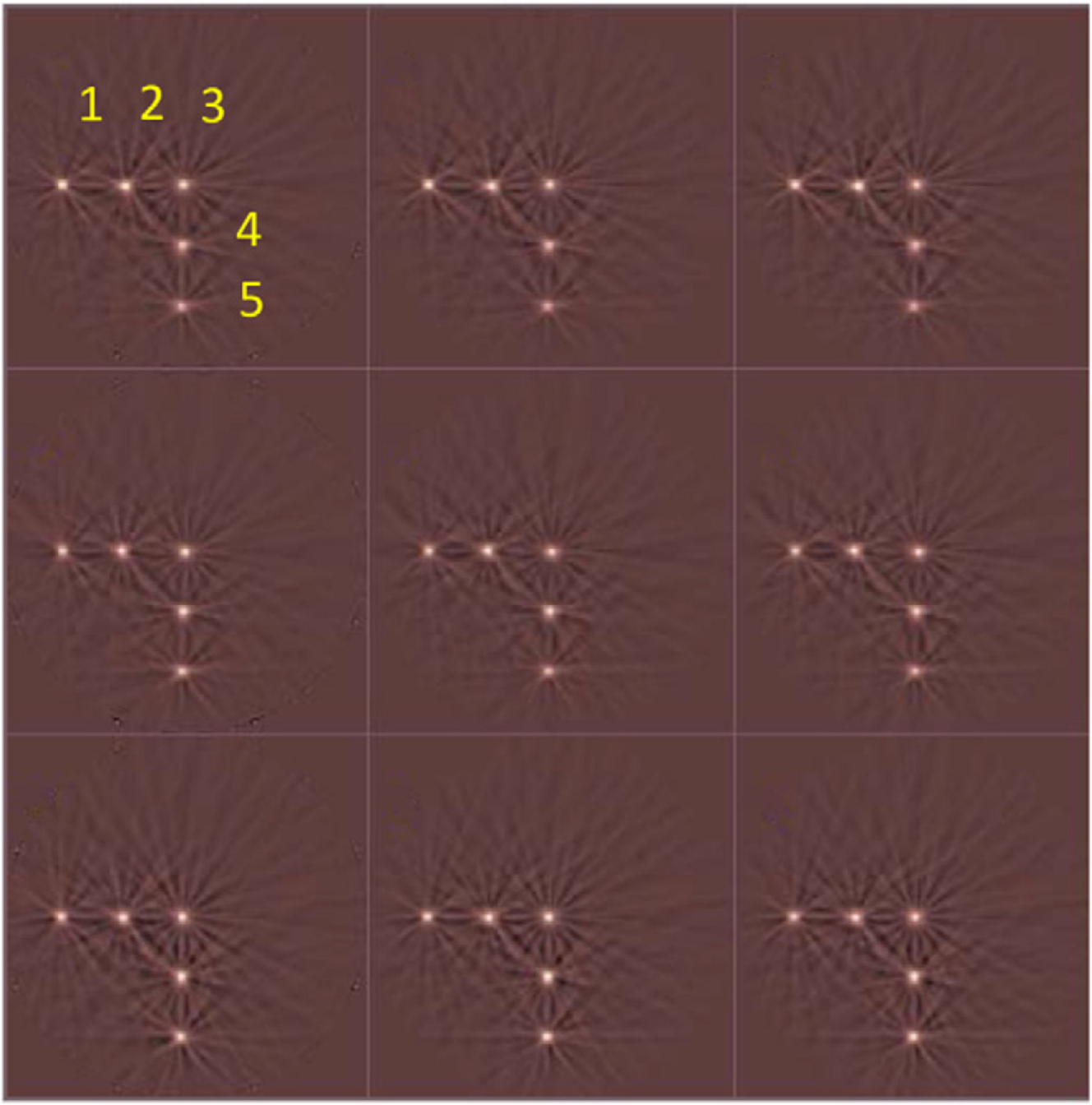

Figure 7.

Reconstructed point source images using different system models. Top row: −¼ axial FOV. Middle row: axial center FOV. Bottom row: +¼ axial FOV. Left column: the accurate model. Middle column: factored model without angular down-sampling. Right column: factored system model with angular down-sampling.

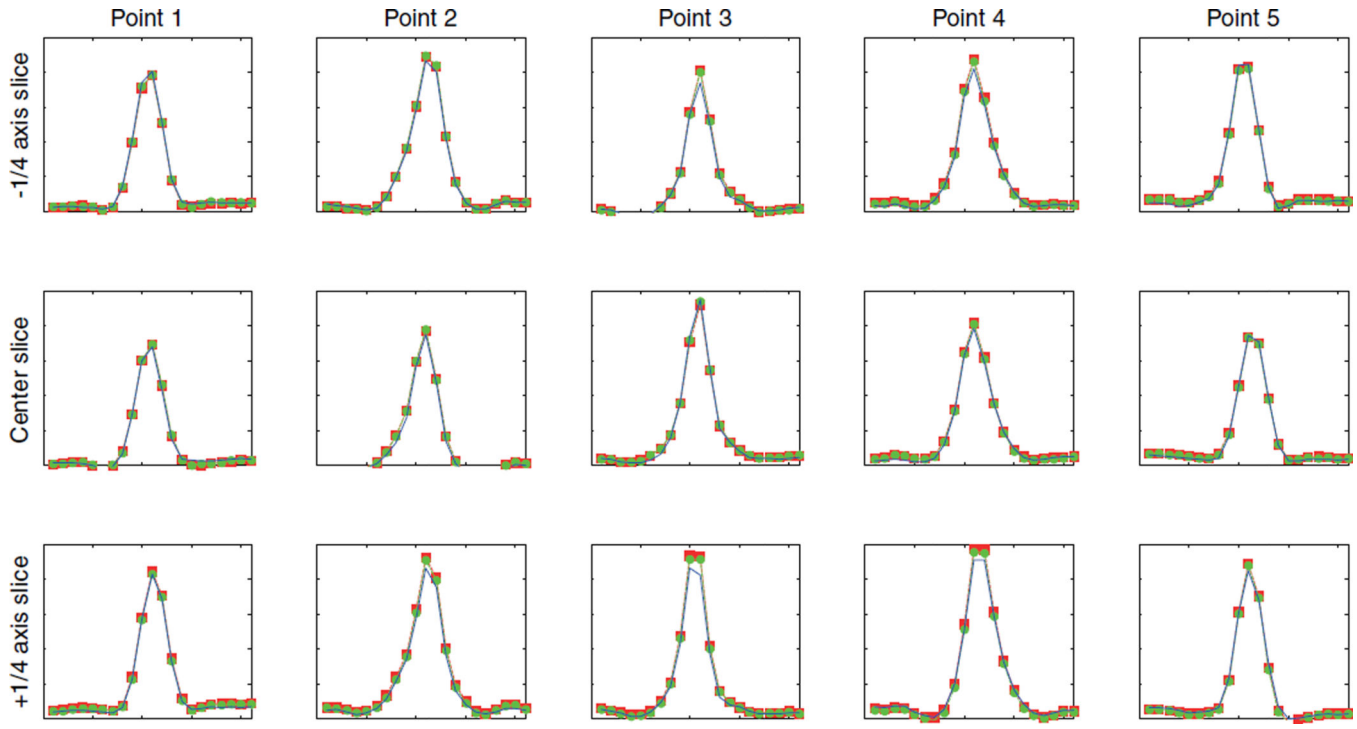

Figure 8.

Reconstructed point source radial profiles. Top row: −¼ axial FOV. Middle row: axial center FOV. Bottom row: +¼ axial FOV. The point source labels are shown in figure 7. Blue solid line: accurate system model. Red square: factored system model. Green circle: factored system model with angular down sampling.

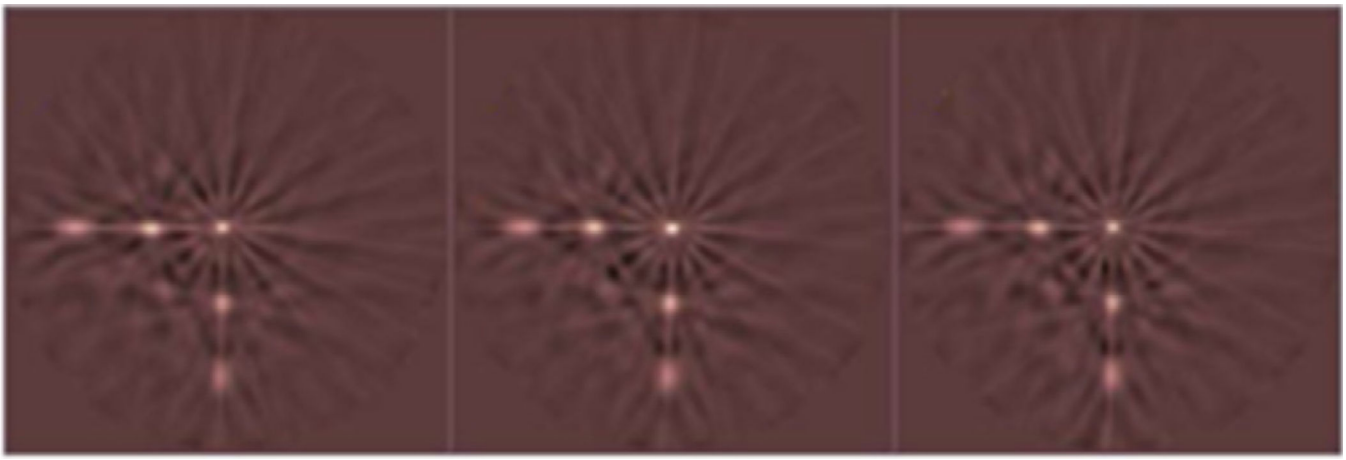

Figure 9.
Reconstructed point source images without DOI information, using the accurate system matrix model. Left to right: −¼ axial FOV, axial center FOV, +¼ axial FOV.

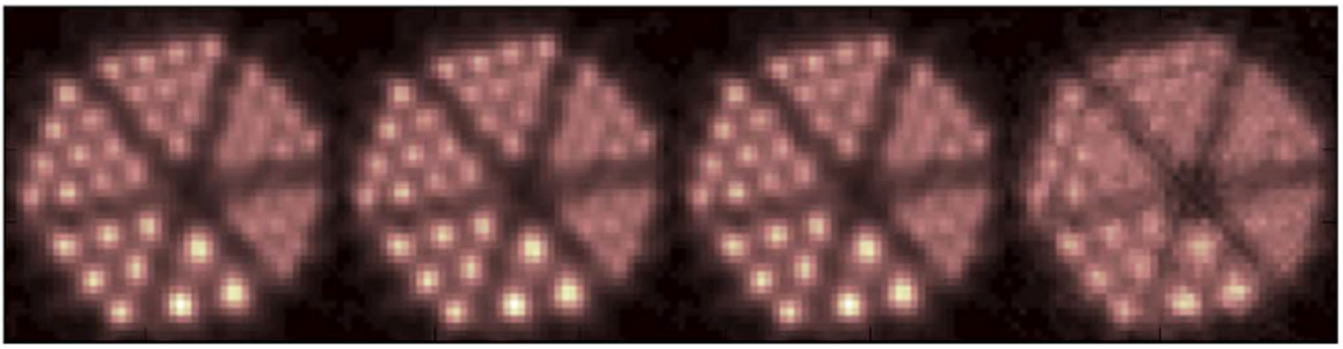

Figure 10.

Reconstructed images of the simulated Derenzo phantom. From left to right: accurate system matrix, factored system matrix, factored system matrix with the angular down-sampling, and without the sinogram blurring matrix.

Table 1

Transaxial resolution for each point source reconstructed using different system models. The point labels are shown in figure 7. The notation ‘P’, ‘BG’ and ‘BG_ds’ denote the accurate, factored and factored with angular down-sampling system models, respectively.

	(a) Radial FWHM (mm)					(b) Tangential FWHM (mm)				
Axial position −¼ axial FOV										
Point source	1	2	3	4	5	1	2	3	4	5
P	0.58	0.56	0.56	0.58	0.60	0.66	0.70	0.54	0.70	0.64
BG	0.58	0.56	0.56	0.60	0.60	0.66	0.70	0.54	0.70	0.62
BG_ds	0.56	0.56	0.56	0.60	0.60	0.66	0.70	0.54	0.68	0.62
Axial position center FOV										
Point source	1	2	3	4	5	1	2	3	4	5
P	0.62	0.62	0.52	0.62	0.66	0.62	0.60	0.56	0.64	0.62
BG	0.62	0.62	0.52	0.62	0.68	0.62	0.62	0.56	0.66	0.62
BG_ds	0.62	0.62	0.52	0.62	0.68	0.62	0.62	0.56	0.64	0.60
Axial position +¼ axial FOV										
Point source	1	2	3	4	5	1	2	3	4	5
P	0.56	0.58	0.58	0.56	0.60	0.62	0.68	0.54	0.70	0.60
BG	0.56	0.58	0.58	0.62	0.62	0.62	0.68	0.56	0.70	0.60
BG_ds	0.56	0.58	0.58	0.62	0.62	0.62	0.68	0.56	0.70	0.60

Table 2

Axial resolution for each point source reconstructed using different system models. The notation ‘P’, ‘BG’ and ‘BG_ds’ denote the accurate, factored and factored with angular down-sampling system models, respectively.

Axial FWHM (mm)					
Axial position −¼ axial FOV					
Point source	1	2	3	4	5
P	0.450	0.450	0.500	0.500	0.475
BG	0.450	0.450	0.525	0.500	0.475
BG_ds	0.475	0.450	0.500	0.500	0.475
Axial position center FOV					
Point source	1	2	3	4	5
P	0.550	0.500	0.500	0.550	0.525
BG	0.525	0.500	0.475	0.550	0.500
BG_ds	0.525	0.500	0.475	0.550	0.500
Axial position +¼ axial FOV					
Point source	1	2	3	4	5
P	0.475	0.475	0.475	0.450	0.500
BG	0.475	0.450	0.475	0.450	0.475
BG_ds	0.475	0.450	0.475	0.450	0.475

Table 3

Transaxial resolution of each point source reconstructed using the accurate system matrix model with different DOI bins.

	(a) Radial FWHM (mm)					(b) Tangential FWHM (mm)				
Axial position −¼ axial FOV										
Point source	1	2	3	4	5	1	2	3	4	5
All DOI bins	0.58	0.56	0.56	0.58	0.60	0.66	0.70	0.54	0.58	0.60
Front 3 DOIs	0.54	0.52	0.52	0.52	0.56	0.60	0.62	0.50	0.52	0.56
No DOI	2.48	1.48	0.78	1.29	2.28	0.70	0.88	0.80	0.64	0.68
Axial position center FOV										
Point source	1	2	3	4	5	1	2	3	4	5
All DOI bins	0.62	0.62	0.52	0.62	0.66	0.62	0.60	0.56	0.62	0.66
Front 3 DOIs	0.54	0.62	0.44	0.56	0.54	0.64	0.54	0.50	0.56	0.54
No DOI	2.36	1.36	0.76	1.26	2.12	0.78	0.84	0.62	0.80	0.76
Axial position +¼ axial FOV										
Point source	1	2	3	4	5	1	2	3	4	5
All DOI bins	0.56	0.58	0.58	0.56	0.60	0.62	0.68	0.54	0.56	0.60
Front 3 DOIs	0.52	0.56	0.54	0.54	0.54	0.64	0.66	0.52	0.54	0.54
No DOI	2.05	1.43	0.78	1.30	2.09	0.86	0.84	0.76	0.76	0.84

Table 4

Comparison of storage size. P, BG and BG_ds represent the accurate, factored and factored with angular down-sampling system models, respectively.

	Size (GB)	Reduction factor
P	14	—
BG	3.2	4.375
BG_ds	1.6	8.75

Table 5

Comparison of projection speed (in seconds). P, BG and BG_ds represent the accurate, factored and factored with angular down-sampling system models, respectively.

Matrix	Forward	Back	Total	Speed up factor
P	86	79	165	—
BG	8(B) + 18(G) = 26	27	51	3.2
BG_ds	4(B) + 10(G) = 14	17	31	5.5